

High-Q Peaks and Nonstationarity in the Deep Ocean Infragravity Wave Band: Tidal Harmonics and Solar Normal Modes

Alan D. Chave¹, Douglas S. Luther² and David J. Thomson³

¹ Department of Applied Ocean Physics and Engineering, Woods Hole Oceanographic Institution, Woods Hole, MA 02543, USA

² Department of Oceanography, JIMAR & SOEST, University of Hawai'i at Mānoa, Honolulu, HI 96822, USA

³Department of Mathematics and Statistics, Queen's University, Kingston, Ontario K7L 3N6, Canada

1

Contents of this file

Text S1 to S5
Figures S1 to S8
Table S1

Additional Supporting Information (Files uploaded separately)

None

Introduction

Text S1 discusses the multitaper spectral estimator used in this study. Table S1 contains the fit of 68 tidal constituents to the pressure record. Figure S1 shows the degrees of freedom, standardized (as described in Section 4.1 in the text) power spectrum over the 400-4000 μHz analysis band and a detailed standardized spectrum over 400-1400 μHz . Figure S2 compares the empirical probability density function of spectral estimates with a mixture non-central/central χ^2 fit to them by the maximum likelihood method over four frequency bands and data intervals. Figure S3 depicts the frequencies where the multitaper F-test exceeds the 0.99 level and is within 2 Rayleighs of the frequency of a harmonic of the tide contained in Table S1. Text S2 provides background information on solar normal modes. Text S3 and Figure S4 shows the two-point coherence between PN2 and nearby site PN3 that demonstrates isotropic propagation of free IGWs. Text S5, along with Figures S5 and S6, describe the standardized spectrum and offset coherence at 2800-2870 μHz over year-day 418-478. Text S5, along with Figures S7 and S8, describe the standardized spectrum and offset coherence at 1175-1225 μHz over year-day 113-173.

Text S1. Multitaper Spectral Estimation

Let a time sequence of data with a fixed sample interval be given by x_t $t = 0, \dots, N - 1$. The discrete Fourier transform of a time sequence is given by

$$y(f) = \sum_{t=0}^{N-1} x_t e^{-i2\pi f t} \quad (\text{S1})$$

and is a trivial sufficient statistic for the time sequence because it can always be recovered by taking the discrete inverse of (S1). For unit sampling, the ordinary frequency f has principal domain $[-1/2, 1/2)$, and f is a continuous variable because the Fourier transform is a holomorphic function over the whole complex plane (i.e., is entire). Consequently, the inverse transform of (S1) is

$$x_t = \int_{-1/2}^{1/2} e^{i2\pi f t} y(f) df \quad (\text{S2})$$

Convert (S1)–(S2) to a time-centered form by replacing t with $t - (N - 1)/2$, and combine (S1) and (1) in the text to yield the fundamental equation of spectral analysis

$$y(f) = \int_{-1/2}^{1/2} \frac{\sin N\rho(f - \eta)}{\sin \rho(f - \eta)} dX(\eta) \quad (\text{S3})$$

The essence of multitaper spectral analysis is treatment of (S3) as an integral equation of the first kind, with $dX(f)$ as the unknown function whose moments are to be estimated, and $y(f)$ as the data. It is well known that first kind integral equations do not have unique solutions, and thus the “best” solution in some specified sense is sought. The criterion used in the multitaper estimator is minimizing the bias outside an interior domain $[-W, W]$, where W is a free parameter that specifies the resolution bandwidth $2W$ of a multitaper estimate.

The kernel function in (S3) is the Dirichlet kernel whose eigenfunctions are the Slepian functions (Slepian, 1978) $U_k(N, W; f)$ that are orthonormal on $[-1/2, 1/2]$ and orthogonal on $[-W, W]$. The Dirichlet kernel eigenvalues l_k give the fractional energy concentration in $[-W, W]$. The Fourier transforms of the Slepian functions are the Slepian sequences $v_t^k(N, W)$ that serve as data tapers in multitaper estimates.

The derivation of the multitaper power spectrum estimate using a Slepian function basis is described in Thomson (1982) and Percival and Walden (1993, Ch. 7). The form used in this work for the spectrum averaged over the interior domain is

$$\bar{S}(f) = \frac{\hat{a}_{k=0}^{K-1} l_k d_k^2(f) \hat{S}_k(f)}{\hat{a}_{k=0}^{K-1} l_k d_k^2(f)} \quad (\text{S4})$$

where $K \leq \lfloor 2NW \rfloor$ depends on the time-bandwidth product NW , and the data-adaptive weights are given by

$$d_k(f) = \frac{\sqrt{l_k} S(f)}{l_k S(f) + S^2(1 - l_k)} \quad (\text{S5})$$

The $\{\hat{S}_k(f)\}$ are direct estimates computed using the k -th Slepian sequence as a data taper, and S^2 is the population variance. A spectrum estimate is obtained by substituting (S5) into (S4), replacing the population entities $S(f)$ and S^2 with estimates and iteratively solving the resulting nonlinear equation. Once the weights are determined, the degrees of freedom is given by

$$h(f) = 2\hat{\alpha}_{k=0}^{K-1} \lambda_k d_k^2(f) \quad (S6)$$

The adaptive weights (S5) are large at frequencies where bias from outside the interior domain is small, and vice versa. In practice, better performance is achieved after prewhitening using a short autoregressive filter, and K is set to the value $2\lfloor NW \rfloor - 1$.

Deterministic components such as the tides in the multitaper spectrum can be statistically evaluated using an F-test, and can be removed from the stochastic part of the spectrum because the orthogonal Slepian functions define the shape of a line. In this context, deterministic means a process whose bandwidth is small compared to the resolution bandwidth of the estimate and whose phase remains substantially constant over the analysis interval. The details can be found in Thomson (1982) and Percival and Walden (1993).

The Loève spectrum is presented as the offset magnitude squared coherence

$$\hat{g}^2(f, f') = \frac{\sum_{k=0}^{K-1} \lambda_k |d_k(f) d_k(f + f') \hat{a}_k(f) \hat{a}_k(f + f')|^2}{\bar{S}(f) \bar{S}(f + f')} \quad (S7)$$

where f is the ordinary frequency, f' is the offset frequency, $d_k(f)$ is given by (S5), λ_k is the eigenvalue for the k -th Slepian sequence, $\hat{a}_k(f)$ is the Fourier transform of the time series using the k -th Slepian sequence as a data taper, $\bar{S}(f)$ is given by (S4), $K = 2NW - 1$ is the number of Slepian tapers utilized, N is the length of the time series and $2W$ is the user-specified resolution bandwidth of the estimate.

Text S2. Solar Normal Modes

Some types of internal motions of both Earth and Sun are described by normal modes that are characterized using a spherical harmonic expansion indexed by “quantum numbers” n , l and m . The radial order n gives the number of zeros along a radial line, while the degree l denotes the number of nodal lines in latitude. The azimuthal order m is the number of nodal lines in longitude, with $-l \leq m \leq l$, and is a consequence of rotation of Earth or Sun. A given normal mode is characterized by its frequency f and quality factor Q , with the latter defined as the ratio of the center frequency to the full bandwidth at half power.

There are two families of normal modes of Earth: the spheroidal ${}_nS_l$ and toroidal ${}_nT_l$ ones (Dahlen and Tromp, 1998), but only the former would be expected to be present in the seafloor pressure field. The spheroidal modes exist over the frequency range $\sim 300\text{--}10,000$ μHz , and, with the exception of ${}_0S_0$, their Q 's are typically a few hundred, decreasing with increasing frequency. Ocean resonances have substantially lower Q 's, with typical values being 10 or less except for diurnal and semidiurnal tidal resonances, where they are about a factor of two larger.

Over the frequency range considered in this paper, there are three classes of solar normal modes: the gravity $g_{n,l,m}$, fundamental $f_{l,m}$ and pressure $p_{n,l,m}$ ones. For a recent review of the study of these modes, or helioseismology, see Christensen-Dalsgaard (2002). The restoring force for gravity modes is buoyancy, and they are analogous to internal waves in the ocean. They have frequencies $\lesssim 400$ μHz (periods longer than ~ 0.7 h), but have not been observed optically. The fundamental modes are analogous to surface gravity waves in the ocean, occur at frequencies $\sim 350\text{--}3000$ μHz , but typically have substantially lower amplitudes than pressure modes at higher frequencies. See Provost et al. (2000) for further details. Avoiding the poorly characterized g-modes is the motivation for restricting this study to frequencies above 400 μHz .

The pressure or p-modes are solar acoustic standing waves in the frequency range extending from ~ 250 μHz to the acoustic cutoff at ~ 5100 μHz , or periods from about an hour to a few minutes. Their frequencies are given asymptotically by

$$\omega_{n,l,m} \approx m\omega_r + \omega_o \left[(l+1/2) / 2 + n + \alpha \right] \quad (\text{S8})$$

where $\eta_o \gg 135 \mu\text{Hz}$, the rotational splitting term $\eta_r \gg 440 \text{ nHz}$ and α is the turning point phase shift (as a fraction of π) that depends weakly on frequency. Given (S8), the p-modes are densely packed above $\sim 2000 \mu\text{Hz}$, with about 100 modes per μHz when all possible rotational splitting terms are included, and so it is potentially increasingly difficult to identify a given mode in spectra with rising frequency. The frequencies of the p-modes change slightly with solar activity, especially at higher frequencies (Woodard & Noyes, 1985; Chaplin et al., 2000). P-modes are probably excited by turbulence in the solar convection zone (Moretti et al., 2001), and hence their amplitudes are random and nonstationary. The Q 's of p-modes are several thousand, and increase with frequency. As a consequence, a given mode persists for 1–2 months, and the power spectrum of a measurement driven by them is a function of time. In addition, their frequencies can vary by $\sim 1 \mu\text{Hz}$ from their nominal values, as has been shown through optical measurements.

An important characteristic of p-mode production is that about 1/3 of a given area on Sun at a specific time, or of a given time at a specific location on Sun, displays modal activity, with the pattern varying continuously (Stix, 2004, p. 183). Viall et al. (2009) showed that for about half of solar wind data segments exhibiting a p-mode peak, a statistically significant corresponding peak was present in magnetospheric data. Combining these observations, it is reasonable to expect a given mode to be observed on Earth about 1/6 of the time. Given that persistence of an excited mode is $O(1 \text{ month})$, this suggests substantial nonstationarity that will have to be accommodated in the data analysis strategy.

P-modes have been observed optically for the past thirty years at frequencies above $1000 \mu\text{Hz}$, but the data are less reliable below that value. Results from the Michelson Doppler Imager (MDI) on the Solar and Heliospheric Observatory (SOHO) satellite are used for reference in this study at frequencies above $1000 \mu\text{Hz}$; see Scherrer et al. (1995) for a description of MDI and Rhodes et al. (1997) for initial results. At frequencies below $1000 \mu\text{Hz}$, Provost et al. (2000) provide mode frequencies, many of which are the result of model calculations.

Text S3. Coherence and Phase with a Nearby Pressure Record

Figure S4 shows the coherence and its phase for the PN2 pressure record with a second PN3 data set that is located 236 km distant at 26°49.3'N, 164°19.3'W. The analysis interval extends from 04.05.2001 through 14.05.2002. This is a conventional band-averaged estimate with the averaging bandwidth increasing with frequency, as shown by the green 95% confidence level curve. The variable resolution bandwidth in this estimate is too large to resolve individual solar modes, but does serve to establish the presence of propagating IGWs in the pressure data regardless of the energy source.

Under a model of random waves propagating in a horizontal plane with different directions, but with similar magnitudes in all directions and the same phase velocity for a given frequency, Aki (1957, 1965) showed that the coherence between two measures of the wave field is independent of the azimuth of one station relative to the other and proportional to the magnitude of a first kind Bessel function $\left| J_0(kr) \right|$, where k is the horizontal wavenumber that obtains from the gravity wave dispersion relation and r is the distance between the measures. The predicted Bessel function for an isotropic field of rotation-modified gravity waves is superimposed in red on the coherence in Figure S4. The coherence matches quite well with the predicted coherence function at frequencies as high as ~2000 μHz ; note also that the phase flips at zeros in the Bessel function. The lower than predicted observed coherence at frequencies higher than ~1000 μHz is most likely due to the increasing influence of highly directional IGWs coming out of the Vancouver Island area, as described in Filloux et al. (1991). The coherence minima at ~7, ~10 and ~15 hours are probably due to internal waves that are incoherent across the intersensor distance. This figure provides strong evidence for free IGWs in the analysis frequency band of this paper regardless of their origin.

Text S4. Standardized Spectrum and Offset Coherence over 2800-2870 μHz

Figure S5 shows the power spectrum over 2800-2870 μHz (central period of ~353 s) for a 60 d data block ranging from year-day 418-478, or early spring 2002. There are two peaks that exceed 8 standard deviations from the noise floor, an additional peak that exceeds 6 standard deviations and an additional three peaks that exceed 4 standard deviations. There is one additional peak that nearly reaches the 4 σ level. The probabilities of a single peak exceeding 8 σ [6 σ] (4 σ) are 3.1×10^{-6} [2.2×10^{-4}] (0.0097), respectively,

for a central C_{18}^2 variate. Consequently, the probabilities of observing two independent peaks at 8σ is 9.6×10^{-12} , three independent peaks at 6σ is 1.1×10^{-11} and six independent peaks at 4σ is 8.3×10^{-13} , respectively. Any of these scenarios is extremely unlikely, and hence one has to conclude that there is a non-random forcing component present at one or more frequencies. The occurrence of peaks near the center ($m = 0$) frequency of many solar p-modes is suggestive of their origin. These peaks have the characteristic rectangular shape of a quasi-deterministic component in a multitaper estimate, with the possible exception of the one centered at ~ 2827 μHz that has a more triangular shape characteristic of a random peak. However, a random peak at the 8σ level is difficult to accept. Further, the full bandwidth at half power of the two largest peaks in Figure S5 is respectively 3 and 2 μHz , which is close to the resolution bandwidth of the estimate and not as large as would be expected for a random peak. The peak widths imply a Q of at least 1400, vastly exceeding that of any oceanic or atmospheric process. The smaller peaks in Figure S5 also display a bandwidth commensurate with that of the estimate, and so also represent high Q processes.

The locations of the ${}_3S_8$ and ${}_6S_3$ terrestrial spheroidal normal modes taken from Masters and Widmer (1995) are also marked in Figure S5. The Q s of these modes are given as 303 and 448, which correspond to full bandwidths at half power of 9 and 6 μHz , respectively. However, neither of these frequencies is associated with major peaks in the spectrum, and there are no spectral features with such high bandwidths, so it is unlikely that these modes are present in the data.

Figure S6 shows the offset coherence corresponding to Figure S5. The most prominent feature is the trapezoidal pattern centered at zero offset frequency extending over ~ 2834 - 2842 μHz , with considerable internal fine structure spaced at offset frequencies ~ 400 nHz. This feature corresponds to a sequence of 5σ or larger peaks in Figure S5. The pattern is coherent at offset frequencies of $+11.6$ - 19 μHz that corresponds to the narrow peak at ~ 2853 μHz in Figure S5, and at negative offset frequencies that encompass the high power interval from ~ 2818 - 2831 μHz . In fact, the 2853 μHz peak is also coherent with 2826 μHz , which is the first 8σ peak in Figure S5. Curiously, the peak in Figure S5 at ~ 2843 μHz does not display any coherence with other frequencies, but might be correlated with features outside the analysis band.

Text S5. Standardized Spectrum and Offset Coherence over 1175-1225 μHz

Figure S7 shows the power spectrum over 1175-1225 μHz for year-days 113-173, or late spring 2001. There are two peaks in the figure that are 6σ above the noise level, and two more that substantially exceed 5σ from that value. The probabilities for 6σ (5σ) peaks in a central C_{18}^2 population are 0.019 (0.05), respectively, and so the probabilities of independently observing two 6σ peaks (four 5σ peaks) is 3.6×10^{-4} (6.3×10^{-6}), both of which are unlikely, hence requiring the presence of quasi-deterministic forcing.

All of the large peaks (and in addition most of the smaller ones) have a full bandwidth at half power of ~ 2 μHz , or the resolution bandwidth of the estimate. As a result, their Q s are at least 600. Most of these peaks occur near the center frequency of low radial order solar p-modes. The exception is the two symmetric peaks around the one labeled $p_{0,142}$, which are at ± 3 μHz from it.

However, the same two peaks might be attributed to tidal harmonics. The multitaper F-test is significant at the 0.99 level near the center frequency in both cases. The 1202 μHz peak is within $1\mathcal{R}$ of the 100th harmonic of J1 and $1.8\mathcal{R}$ of the 52nd harmonic of T2. The 1208 μHz peak is within $0.7\mathcal{R}$ of the 108th harmonic of M1, $1.3\mathcal{R}$ of the 97th harmonic of OO1, and $1.6\mathcal{R}$ of the 56th harmonic of $\mu 2$.

Figure S8 shows the offset coherence for the same time and frequency interval as for Figure S7. The most prominent feature is the trapezoidal patch of coherence extending from 1200-1206 μHz at zero offset frequency that is outlined by red dotted lines. This corresponds to the peak labeled $p_{0,142}$ and the left symmetric peak in Figure S7. There is coherence of this patch at an offset frequency of $+17.5$ μHz that corresponds to the rightmost peak in Figure S7 that is reflected as coherence at 1220 μHz that displays offset coherence at -17.5 μHz ; both patches are outlined by ovals in Figure S8. There are also numerous peaks at the 2-3 level throughout Figure S8, and given that these have the 0.99 to 0.999 probability level, there are far more of them than should occur at random.

Additional References

Aki, K. (1965), A note on the use of microseisms in determining the shallow structures of the earth's crust. *Geophysics*, 30, 665-666.

Chaplin, W.J., Appourchaux, T., Elsworth, Y., Isaak, G.R., Miller, B.A., & New, R., (2000), Source of excitation of low-l solar p modes: Characteristics and solar-cycle variations. *Mon. Not. R. Astr. Soc.*, 314, 75-86.

- Dahlen, F.A., & Tromp, J. (1998), *Theoretical Global Seismology*. Princeton: Princeton Univ. Press.
- Moretti, P.F., Cacciani, A., Hanslmeier, A., Messerotti, M., Oliviero, W., Ortuba, W., Severino, G., & Warmuth, A. (2001), The source of solar oscillations: Convective or magnetic. *Astron. Astrophys.*, 372, 1038-1047. <https://doi.org/10.1051/0004-6361:20010588>
- Percival, D.B., & Walden, A.T. (1993), *Spectral Analysis for Physical Applications*. Cambridge: Cambridge U. Press.
- Scherrer, P.H., Bogart, R.S., Bush, R.I., Hoeksema, J.T., Kosovichev, A.G., Schou, J., Rosenberg, W., Springer, L., Tarbell, T.D., Title, A., Wolfson, C.J., Zayer, I. & the MDI Engineering Team (1995), In Fleck, B., Domingo, V. & Poland, A. (eds), *The Soho Mission*, Dordrecht: Springer.
- Slepian, D. (1978), Prolate spheroidal wave functions, Fourier analysis and uncertainty-V. The discrete case. *Bell. Sys. Tech. J.*, 57, 1371-1430. <https://doi.org/10.1002/j.1538-7305.1978.tb02104.x>
- Stix, M. (2004), *The Sun: An Introduction*, 2nd ed. Berlin: Springer-Verlag.
- Thomson, D.J. (1982), Spectrum estimation and harmonic analysis. *Proc. IEEE*, 70, 1055–1096. <https://doi.org/10.1109/Q14PROC.1982.12433>
- Woodard, M.F., & Noyes, R.W. (1985), Change in solar oscillation eigenfrequencies with the solar cycle. *Nature*, 318, 449-450. <https://doi.org/10.1038/318449a0>

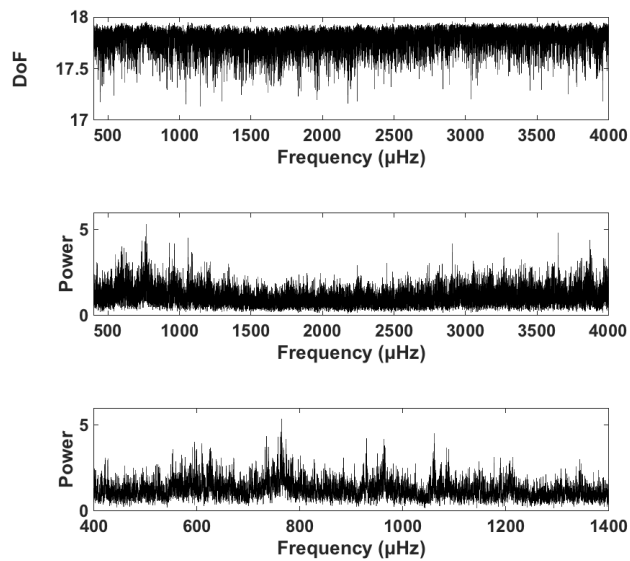


Figure S1. Degrees of freedom against frequency (top panel), standardized power spectral density against frequency over 400-4000 μHz (middle panel) and standardized spectral density over 400-1400 μHz (bottom) for the high pass filtered pressure record. The time-bandwidth is 5 and 9 tapers were used, yielding an average of 17.8 degrees of freedom per frequency and a resolution bandwidth of 0.30 μHz . Standardizing comprises fitting a quadratic polynomial to log frequency-log power over 200-4000 μHz and removing it.

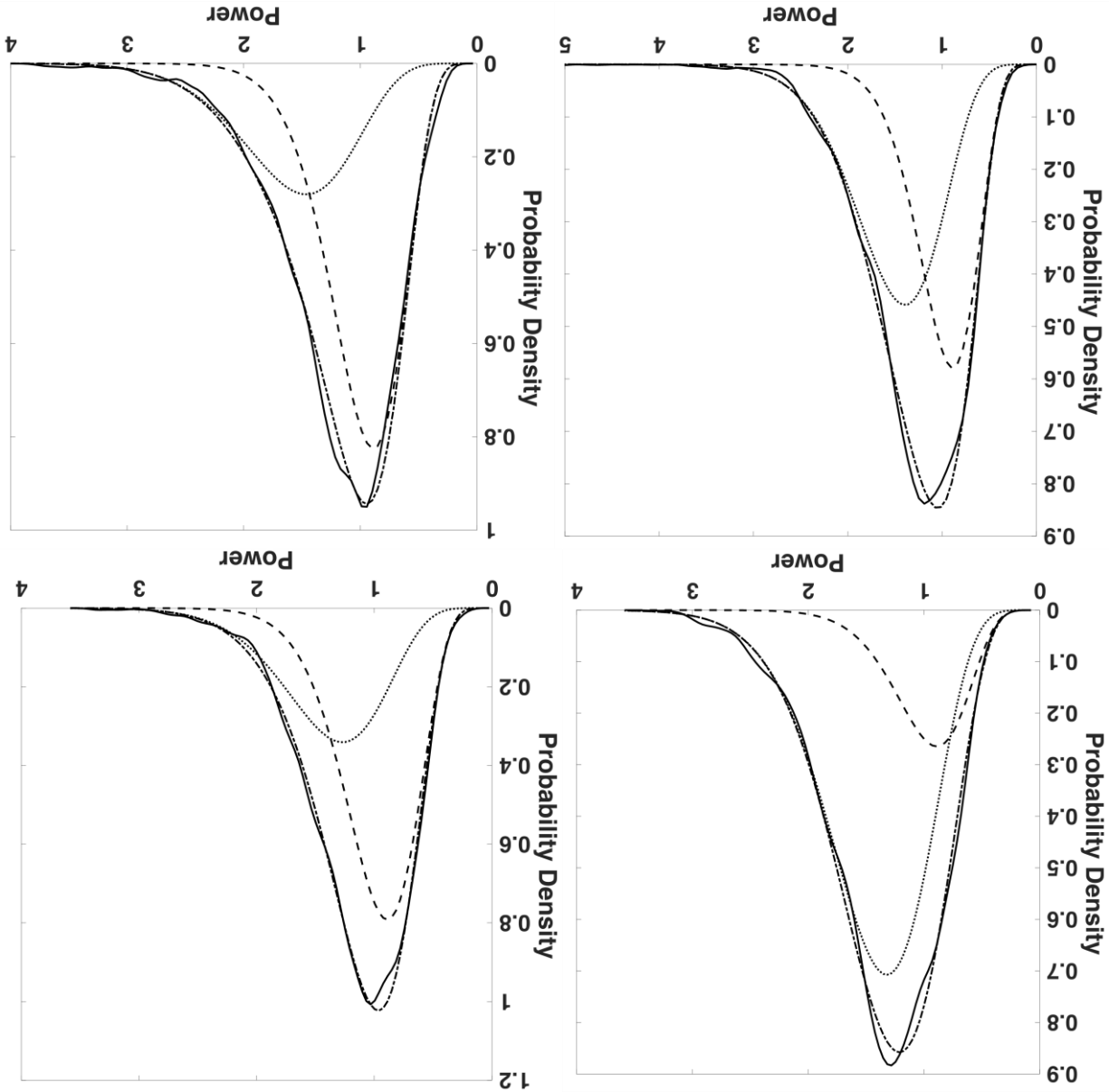


Figure S2. The kernel density empirical distribution for the mixture model (5) in the text fit to multitaper spectral estimates (solid line) along with the mixture model fit (dot-dash line), the central χ^2 component (dashed line) and the non-central χ^2 component (dotted line). From the top left and proceeding clockwise, the panels show the 400–1000 μHz fit for a central year-day of 268 (early fall), the 800–1400 μHz fit for a central year-day of 208 (mid-summer), the 2500–3500 μHz fit for a central year-day of 268 (early fall) and the 3000–4000 μHz fit for a central year-day of 418 (mid-winter).

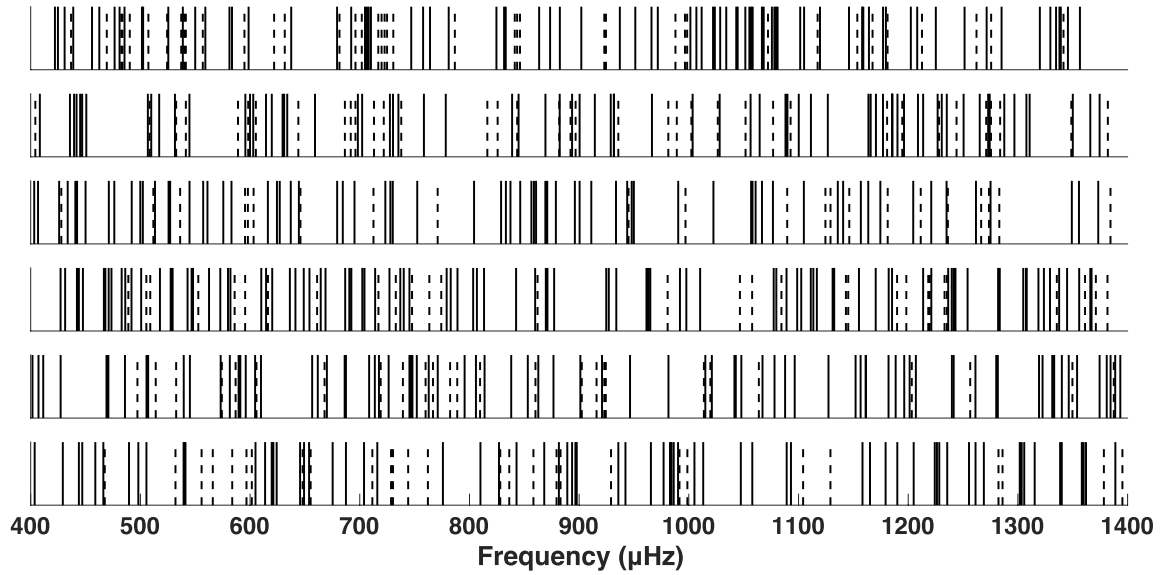


Figure S3. Frequencies where the multitaper F-test exceeds the 0.99 level and is within 0-1 \mathcal{R} (solid line) and 1-2 \mathcal{R} (dashed line) of the frequency of a harmonic of the tide set described in the text. From top to bottom, the six panels are for 60 d abutting data sections with center year-days of 143, 208, 268, 328, 388 and 448 relative to 01.01.2001. The time-bandwidth is 6 and 11 data tapers were used.

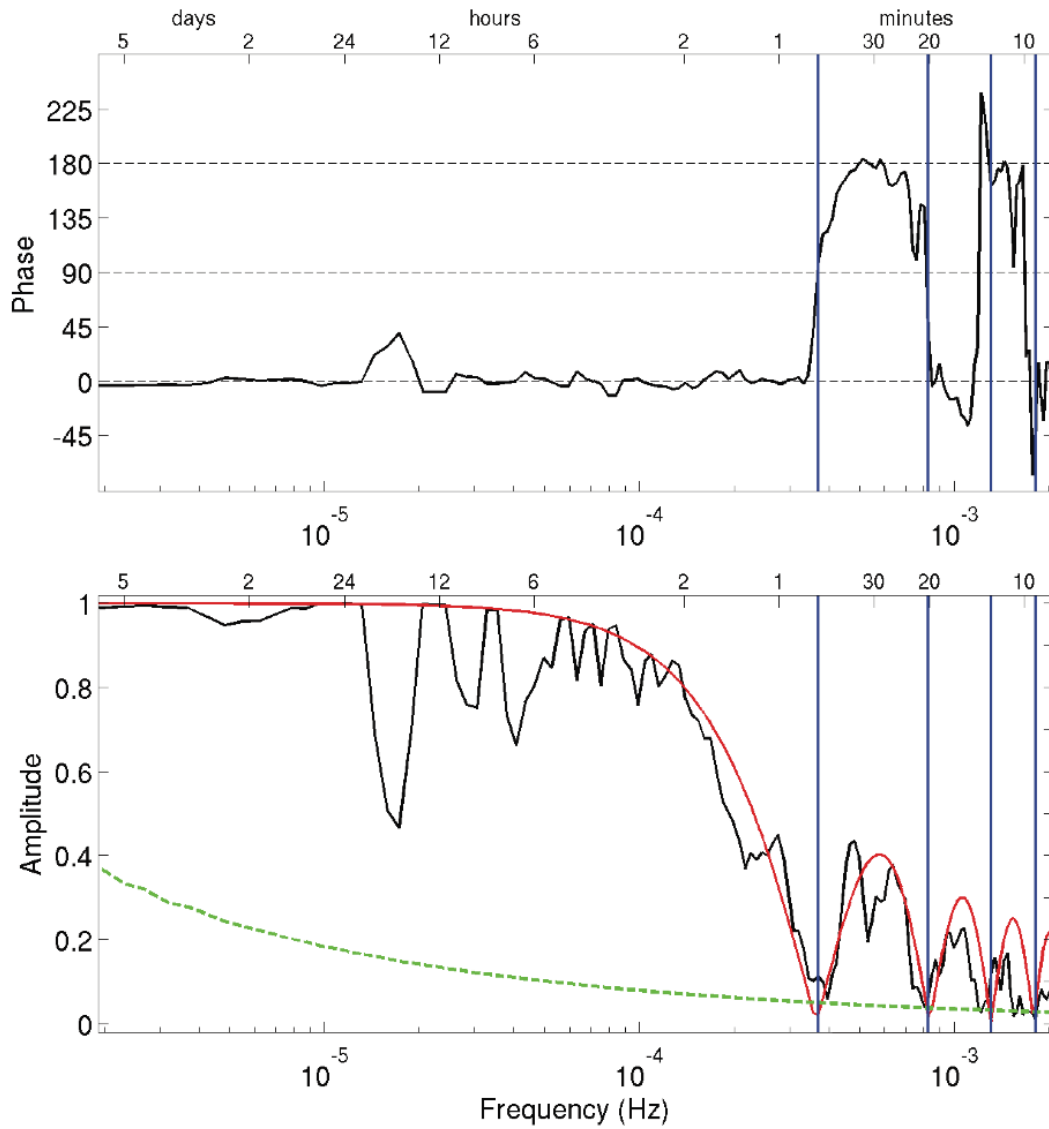


Figure S4. The band-averaged coherence (bottom panel) and its phase (top panel) for the bottom pressure at site PN2 with nearby site PN3 (see text for details). The averaging bandwidth increases with frequency, as shown by the green 95% confidence level relative to the abscissa. The Bessel function model coherence described in the text is superimposed as the red curve in the bottom panel. The vertical lines denote the zero crossings of the Bessel function.

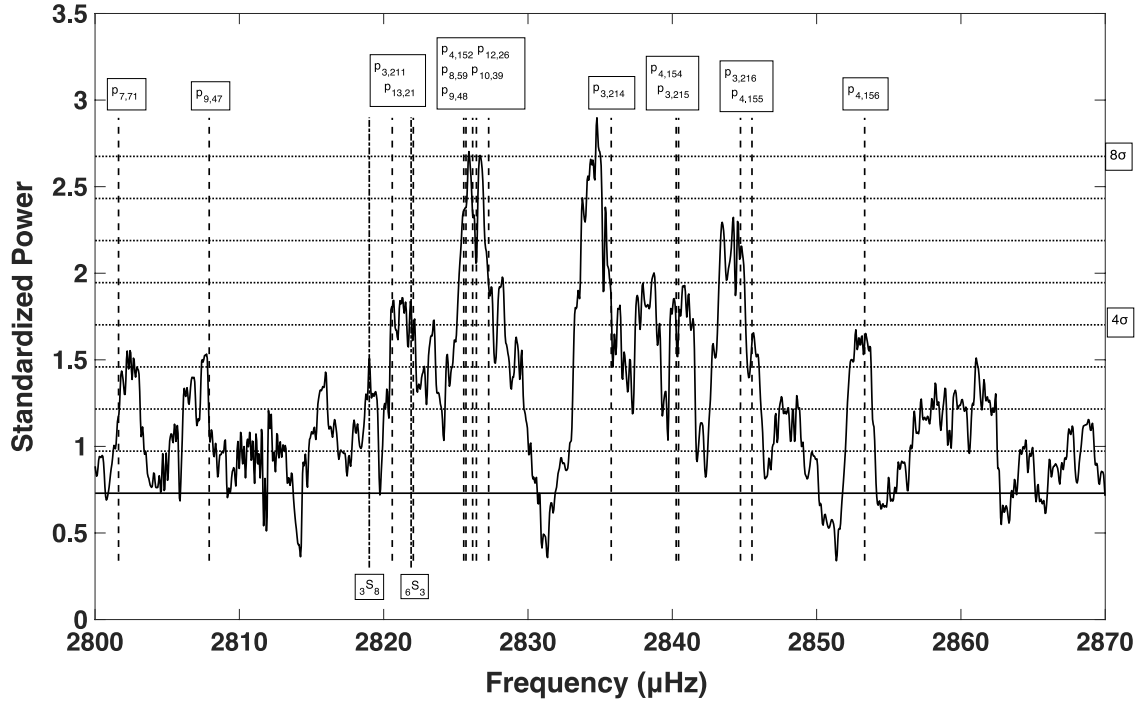


Figure S5. Standardized power spectral density versus frequency on linear scales over year-day 418-478. The time-bandwidth is 5 and there are 9 data tapers, yielding a resolution bandwidth of 1.9 μHz and 18 degrees of freedom per frequency. The solid horizontal line is the 0.1 quantile of power over the 2800-2870 μHz band that defines the noise level, and the dotted horizontal lines are increments of 1 standard deviation from that value, with the 4 and 8σ levels labeled on the right. The vertical dashed lines show the locations of solar p-modes, excluding rotational splitting, as listed at the top, and dash-dot lines denote the location of terrestrial spheroidal normal modes labeled at the bottom.

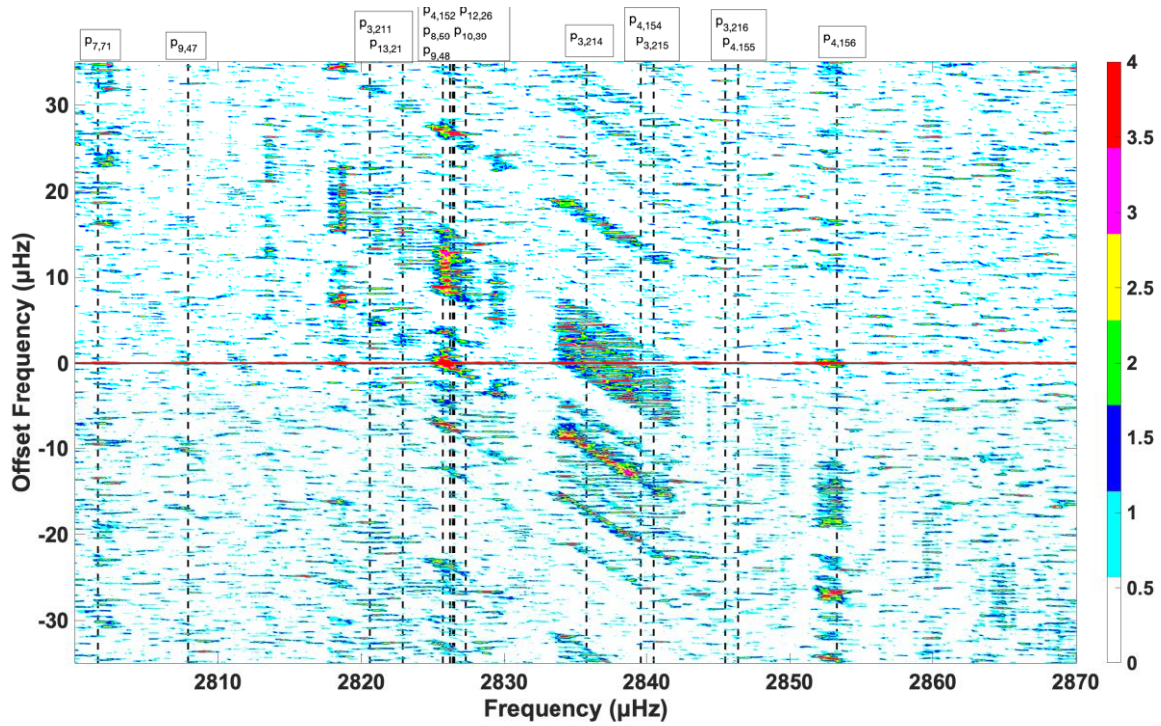


Figure S6. Contours of the offset coherence transformed using (8) in the text against frequency on the abscissa and offset frequency on the ordinate over 2800-2870 μHz for year-days 418-478. The time-bandwidth is 5 and 9 Slepian tapers were used, yielding 18 degrees of freedom per frequency. The vertical dashed lines are the center frequencies for the solar normal modes listed at the top.

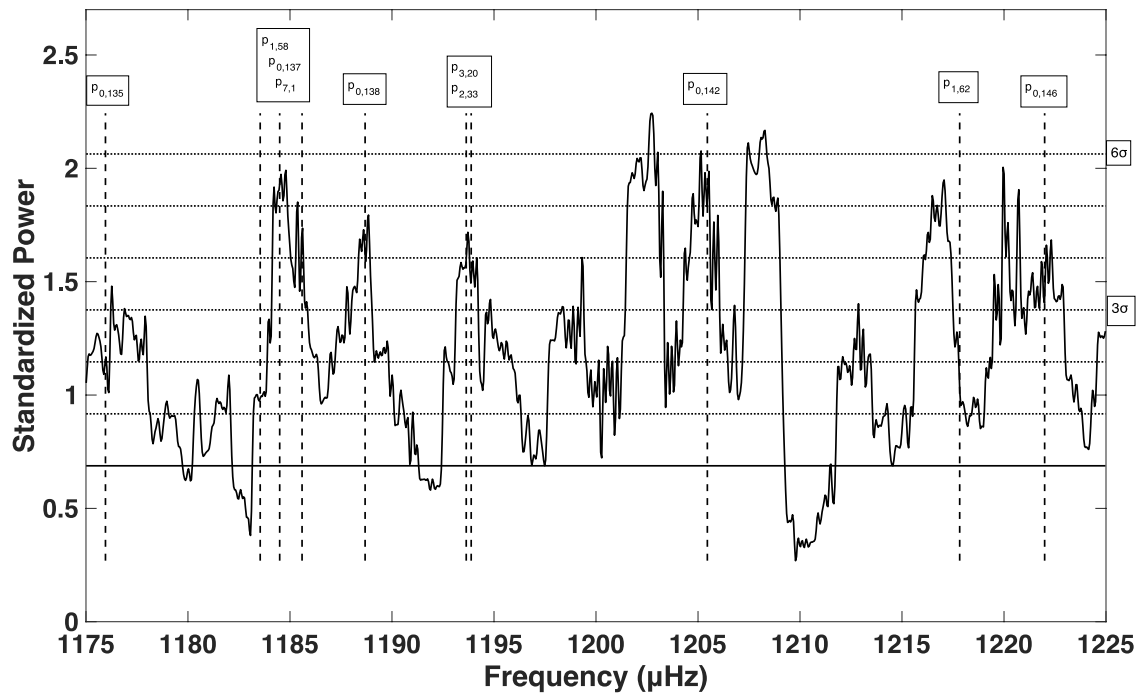


Figure S7. Standardized power spectral density versus frequency on linear scales over year-day 113-173. The time-bandwidth is 5 and there are 9 data tapers, yielding a resolution bandwidth of 1.9 μHz and 18 degrees of freedom per frequency. The solid horizontal line is the 0.1 quantile of power over the 1175-1225 μHz band that defines the noise level, and the dotted horizontal lines are increments of 1 standard deviation from that value, with the 3 and 6 σ levels labeled at right. The vertical dashed lines show the locations of solar p-modes, excluding rotational splitting, as listed at the top.

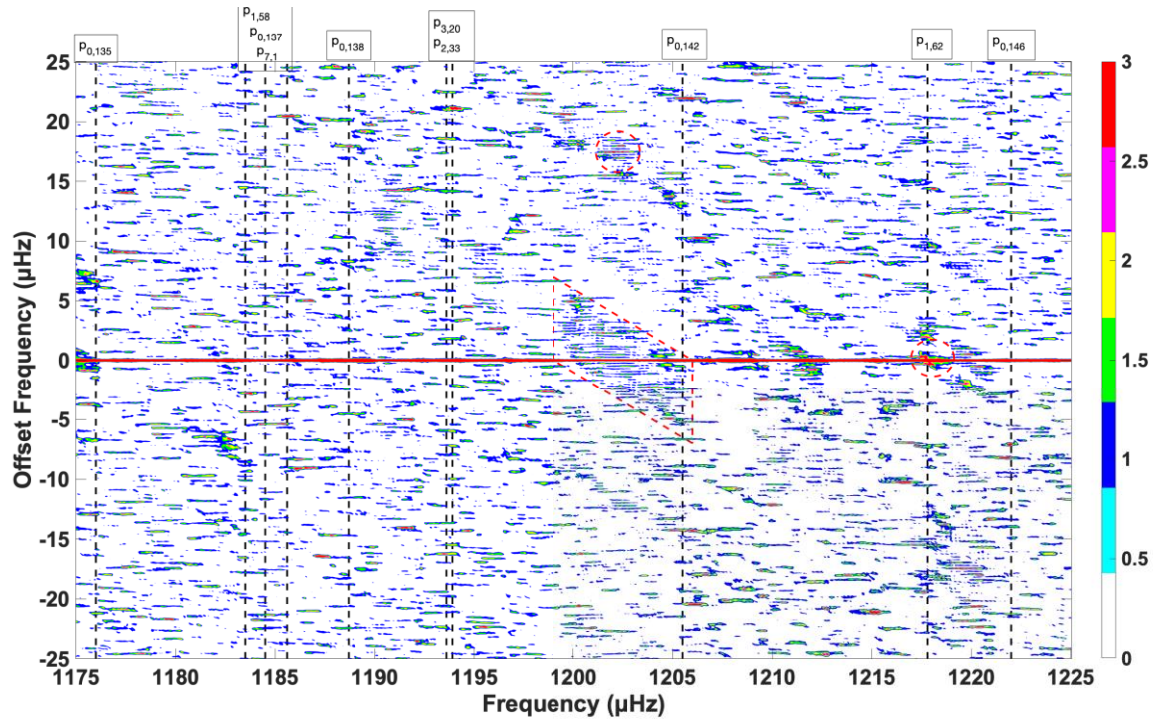


Figure S8. Contours of the offset coherence transformed using (8) in the text against frequency on the abscissa and offset frequency on the ordinate over 1175-1225 μHz for year-days 113-173. The time-bandwidth is 5 and 9 Slepian tapers were used, yielding 18 degrees of freedom per frequency. The vertical dashed lines are the center frequencies for the solar normal modes listed at the top. The red dashed lines delineate features described in the text.

Constituent	Doodson Number	f (μHz)	Amp (Pa)	Error (Pa)	Greenwich Phase	Error ($^\circ$)
SA	056554	0.031687250	171.3	47.7	233.9	15.1
SSA	057555	0.063377528	107.0	45.6	139.6	52.0
MSM	063655	0.363828000	80.5	44.9	227.9	37.1
MM	065455	0.420042167	81.5	43.3	356.2	69.8
MSF	073555	0.783870194	71.0	39.3	244.1	77.5
MF	075555	0.847247722	129.1	49.0	125.8	42.1
$\alpha 1$	117655	9.55460275	8.8	1.9	251.1	12.4
2Q1	125755	9.91843075	17.0	1.8	258.7	6.1
$\sigma 1$	127555	9.97464495	17.8	1.9	235.6	5.8
Q1	135655	10.33847286	156.6	1.8	235.5	0.7
$\rho 1$	137455	10.39468711	27.9	2.0	234.5	3.8
O1	145555	10.75851511	928.9	1.8	234.8	0.1
$\tau 1$	147555	10.82189267	10.3	1.7	205.2	10.9
$\beta 1$	153655	11.12234314	10.7	1.7	282.0	10.9
NO1	155655	11.18572067	77.1	1.7	239.4	1.0
$\chi 1$	157455	11.24193483	17.5	1.8	250.6	6.3
$\pi 1$	162556	11.51069806	30.9	2.2	252.5	3.4
P1	163555	11.54238531	495.2	2.1	239.3	0.2
S1	164556	11.57407558	71.4	2.8	261.3	2.3
K1	165555	11.60576283	1602.9	1.9	242.7	0.1
$\psi 1$	166554	11.63745008	18.7	1.8	264.2	6.3
$\phi 1$	167555	11.66914036	28.1	1.5	232.4	3.9
$\theta 1$	173655	11.96959083	17.7	1.9	260.7	6.2
J1	175455	12.02580503	98.8	2.0	252.1	1.1
SO1	183555	12.38963303	24.9	2.0	278.7	4.5
OO1	185555	12.45510556	62.0	1.8	268.2	1.5

u1	195455	12.87305272	7.4	1.6	287.4	13.9
OQ2	225855	21.10415142	2.3	1.1	303.3	38.3
ϵ 2	227655	21.16036559	11.7	1.2	275.2	6.2
2N2	235755	21.52419361	29.9	1.3	332.2	2.6
μ 2	237555	21.58040778	57.4	1.3	312.7	1.5
N2	245655	21.94423578	248.4	1.4	343.7	0.3
v2	247455	22.00044995	41.7	1.3	339.7	1.7
γ 2	253755	22.30806378	12.1	1.5	5.3	7.2
H1	254556	22.33259072	7.6	1.2	236.6	9.6
M2	255555	22.36427797	1261.2	1.3	346.0	0.1
H2	256554	22.39596522	7.1	1.4	82.5	10.7
MKS2	275555	22.42765550	3.0	1.3	234.6	50.6
LDA2	263655	22.72810597	9.5	1.3	323.7	7.8
L2	265455	22.78432014	31.0	1.3	326.5	2.8
T2	272556	23.11646089	38.8	1.4	343.0	2.0
S2	273555	23.14814814	761.2	1.4	343.1	0.1
R2	274554	23.17983539	12.2	1.0	9.2	5.1
K2	275555	23.21152567	225.9	1.3	342.4	0.3
MSN2	283655	23.56819034	6.6	1.3	130.8	12.1
η 2	285455	23.63156786	13.0	1.2	5.8	5.4
MO3	345555	33.12279306	6.9	0.5	91.3	4.4
M3	355555	33.54641695	23.6	0.5	184.1	1.2
SO3	363555	33.90666334	8.1	0.5	89.6	3.4
MK3	365555	33.97004083	1.8	0.5	99.8	15.1
SK3	383555	34.75391111	35.1	0.5	210.1	0.7
MN4	445655	44.30851361	2.3	0.2	101.0	6.1
M4	455555	44.72855584	10.1	0.3	221.5	1.3
SN4	463655	45.09238389	0.4	0.2	256.5	37.3
MS4	473555	45.51242611	5.0	0.2	11.1	2.4
MK4	475555	45.57580361	1.9	0.2	352.3	6.8

S4	491555	46.29629639	6.4	0.2	89.5	1.9
SK4	493555	46.35967389	1.8	0.2	302.8	7.8
2MK5	565555	56.33431862	2.8	0.1	92.3	2.9
2SK5	5X1555	57.90205917	1.0	0.1	93.4	7.4
2MN6	645655	66.67279167	2.4	0.1	275.1	1.4
M6	655555	67.09283389	3.8	0.1	334.9	0.9
2MS6	673555	67.87670417	4.7	0.1	31.6	0.7
2MK6	675555	67.94008167	2.5	0.1	18.4	1.5
2SM6	691555	68.66057417	1.5	0.1	68.7	2.6
MSK6	693555	68.72395167	1.0	0.1	72.4	3.6
3MK7	765555	78.69859667	0.5	0.0	158.9	2.5
M8	855555	89.45711195	0.8	0.0	181.9	1.8

Table S1. Tidal Constituents for HOME PN2

Data Set S1. Seafloor pressure data in pascals from site PN2 collected during the Hawaii Ocean Mixing Experiment in 2001-2 are contained in an attached ascii file with one value per line. The launch position of the instrument was 26°52.5'N, 161°56.7'W at an uncorrected water depth of 5235 m. The first datum is at 22.04.2001 at 0323:00 GMT and the data are thereafter sampled at 64/h or with a sample interval of 28.125 s. The data were edited to correct minor problems, time corrected under the assumption of a linear clock drift and de-creeped to remove long term drift as described in Filloux (1971, 1980, 1983).